High-throughput high-dynamic range imaging by spatiotemporally structured illumination

TAESEONG WOO,[1] HYE YUN KIM,[2] SU YEON KIM,[3,4] BYUNGJAE HWANG,[1] CHEOLWOO AHN,[1] SEOK-KYU KWON,[3,5] JAE-ICK KIM,[2] AND JUNG-HOON PARK[1,*]

[1]*Department of Biomedical Engineering, Ulsan National Institute of Science and Technology (UNIST), Ulsan 44919, Republic of Korea*
[2]*Department of Biological Sciences, Ulsan National Institute of Science and Technology (UNIST), Ulsan 44919, Republic of Korea*
[3]*Brain Science Institute, Korea Institute of Science and Technology (KIST), Seoul, 02792, Republic of Korea*
[4]*Department of Neuroscience, College of Medicine, Korea University, Seoul, 02841, Republic of Korea*
[5]*Division of Bio-Medical Science & Technology, KIST School, Korea University of Science & Technology (UST), Daejeon, 34113, Republic of Korea*

**jh.park@unist.ac.kr*

Abstract: Recent advances in biochemistry and optics have enabled observation of the faintest signals from even single molecules. However, the limited dynamic range (DR) of current detectors prohibit the simultaneous detection of broadly varying signal levels. In other words, for many biological systems where faint and strong signal sources coexist, traditional imaging methods make a compromise and end up choosing a limited target signal range to be quantitatively measured while other signal levels are either lost beneath the background noise or saturated. The DR can be extended by taking multiple images with varying exposures, which however, severely restricts data throughput. To overcome this limitation, we introduce structured illumination high dynamic range (SI-HDR) imaging which enables real time HDR imaging with a single measurement. We demonstrate the wide and easy applicability of the method by realizing various applications such as high throughput gigapixel imaging of mouse brain slice, quantitative analysis of neuronal mitochondria structures, and fast 3D volumetric HDR imaging.

1. Introduction

The information content of an image is limited by the image size (pixel number) and pixel bit depth. Modern analog to digital converters (ADCs) in current scientific grade cameras provide up to 16-bit depth resolution but the true DR is typically around ~20,000:1 at best which is limited by the read noise and full well capacity. To overcome this limitation, methods aiming to improve hardware and software have both been developed to obtain a wider range of luminance in a single image than restricted by the intrinsic DR of a camera, or in other words, to achieve HDR imaging. One of the most widely used HDR imaging methods in photography is to reconstruct a single HDR image by fusing multiple images acquired with different amounts of exposure [1-5]. This approach does not require any additional hardware and simply uses multiple image acquisitions using a single camera. However, the multiple image acquisition requirement fundamentally increases the total acquisition time needed to reconstruct a single HDR image. Furthermore, an optimization step is required to calibrate the range of exposures

needed to capture the entire luminance range which can vary widely between different target samples. To overcome such limitation in terms of temporal resolution, different approaches inducing different amount of exposures to adjacent pixels in a camera have also been developed by applying a specific mask with different transmittance filters [6, 7]. Although this approach enables single shot HDR imaging, custom masks must be designed for each application environment and image quality can be easily affected by noise during the reconstruction process.

HDR imaging holds valuable information not only in photography but also for microscopy. Especially in bio imaging, subcellular organelles of interest are often labelled with organelle-targeting peptide tagged fluorescent proteins [8-12]. Although the fluorescent intensity holds quantitative information about the molecular content, in many imaging experiments, numerous regions of interest (ROIs) of an image are unavoidably saturated to visualize weakly fluorescing structures which restricts further quantitative analysis. To overcome this limitation, controlling the illumination has been shown to be a viable option to extend the DR in fluorescence imaging. For example, controlled light exposure microscopy (CLEM) realized laser scanning microscopy with real-time negative feedback to modulate the illumination laser power using an electro optical modulator [13-17]. Contrary to conventional laser scanning microscopes which apply the same focused laser beam dosage for the entire field of view (FOV), CLEM actively controls the laser exposure time of illumination light to avoid saturation in strongly fluorescent structures. Other real-time HDR imaging methods based on adjusting the detection levels have also been developed by introducing multiple beam splitters in the detection arm of laser scanning microscopes to acquire different range of signals simultaneously [18-20]. Although this method enables real-time HDR imaging by adding several simple detection optics, DR is extended by blocking signals using absorption filters which unavoidably wastes precious fluorescence photons.

In another approach, directly modulating the illumination or detection light is also an attractive solution as spatial light modulators with independently controllable pixels can be used. For example, HDR images can be obtained by applying binary masks in the detection path against saturated areas [21-24]. A real-time HDR method developed by Nayar et al. used a liquid crystal display as an attenuator in front of the imaging lens to adaptively respond to camera refresh rates up to 30 Hz [25, 26]. However, elaborate control of light intensity at single pixel level accuracy which is required for high resolution microscopy could not be implemented in this method due nonoptimal location of the attenuator. Recently, digital micro-mirror devices (DMDs) have shown great potential to enable adaptive light modulation for HDR imaging. Recent works have successfully demonstrated wide luminance imaging using DMDs [27-30]. However, these works focused only on the suppression of saturation and still required multiple image acquisitions to reconstruct a single HDR image which limits applications to dynamic imaging. Furthermore, although saturation suppression was successfully realized, quantitative HDR reconstruction along the entire extended DR was not demonstrated.

Here we demonstrate structured illumination HDR (SI-HDR), a fast customizable HDR imaging method using a DMD to modulate the illumination intensity on a pixel-by-pixel basis for spatially selective excitation that adapts in real-time to the fluorescence distribution of the object. By using the DMD for illumination modulation, the entire fluorescence photon budget is utilized in detection as in conventional widefield fluorescence imaging. The DR of the

reconstructed HDR image is increased by a factor given by the illumination bit-depth of the DMD analog intensity resolution (8-bit). In contrast to conventional HDR imaging where multiple images are acquired with varying exposures, the analog illumination pattern is dynamically modulated on a pixel-by-pixel basis for each image acquisition increasing the signal to noise ratio (SNR) of all image pixels and enabling quantitative analysis for both weak and intense signals simultaneously. The large dynamic range and high SNR combined with fast imaging enables high throughput imaging of high quality large area datasets, e.g. acquiring large FOV (8.285 x 5.623 mm^2) subcellular resolution macroscopic HDR images in exactly the same total acquisition time as conventional widefield imaging. We also demonstrate the importance of HDR imaging in neuronal networks by observing fine mitochondria structures in neuronal cells, where the simultaneous observation of dense/large mitochondria populations in the soma and sparse/small mitochondria in the axon enables automatic segmentation which is not possible via conventional imaging. Furthermore, the method is broad and general and can be applied to all types of widefield illumination imaging methods. For example, we demonstrate the application of HDR HiLo, where we obtain depth sectioned HDR volumes using just two image frames for each acquired plane [31-33].

2. Method

In fluorescence imaging, the emitted fluorescence intensity $I(\vec{r})$ is given by,

$$I(\vec{r}) = [O(\vec{r}) \cdot P] * PSF, \qquad (1)$$

where $O(\vec{r})$, P, and PSF are the object's fluorescence distribution, illumination intensity, and point spread function, respectively. For the usual case where P is spatially homogeneous, the emission is proportional to the object's fluorescence distribution. Unfortunately, in many biological microscopic imaging scenarios, $O(\vec{r})$ can easily extend over a broad range. Thus, we can express $O(\vec{r})$ as a sum of different areas with relatively low, intermediate, and high fluorescence densities, $\vec{r}_1$, $\vec{r}_2$, and $\vec{r}_3$, respectively,

$$O(\vec{r}) = O(\vec{r}_1) + O(\vec{r}_2) + O(\vec{r}_3). \qquad (2)$$

Incident photons on the detector generate photoelectrons proportional to the quantum efficiency of the detector. Here, the maximum number of photoelectrons containable in a single pixel is given by the full well capacity. The number of photoelectrons is then digitized by an ADC which makes up the two dimensional image that we acquire. Modern cameras have high bit-depth ADCs but the limited full well capacity and the baseline noise floor sets the limit on the dynamic range of the acquired images. When the detected light intensity is too high, the measured signal is saturated. On the other hand, when the detected light intensity is too low, the signal is overwhelmed by the read and dark noise. Using cooled scientific grade cameras, the dark noise can become negligible in most experiments. Substituting eqn. (2) to eqn. (1), $I(\vec{r})$ can be expressed as,

$$I(\vec{r}) = I(\vec{r}_1) + I(\vec{r}_2) + I(\vec{r}_3) = [\{O(\vec{r}_1) + O(\vec{r}_2) + O(\vec{r}_3)\} \cdot P] * PSF. \qquad (3)$$

We can see that $I(\vec{r}_1)$ represents ROIs dominated by read noise, $I(\vec{r}_2)$ represents regions within the dynamic range, and $I(\vec{r}_3)$ represents ROIs that have been saturated. In areas $\vec{r}_1$ and $\vec{r}_3$, the linearity between the emitted fluorescence and detected signal is no longer valid forbidding quantitative analysis. However, if P can be arbitrarily modulated as a function of space, the measured image is now expressed as,

$$I_{SI}(\vec{r}) = [O(\vec{r}) \cdot P(\vec{r})] * PSF = [O(\vec{r}_1) \cdot \alpha(\vec{r}_1) \cdot P + O(\vec{r}_2) \cdot P + O(\vec{r}_3) \cdot \beta(\vec{r}_3) \cdot P] * PSF \quad (4)$$
$$(\text{where } \alpha(\vec{r}_1) > 1 \text{ and } 0 < \beta(\vec{r}_3) < 1).$$

In contrast with $I(\vec{r})$ acquired by homogeneous illumination P, morphological features at $\vec{r}_1$ and $\vec{r}_3$ can now be retrieved simultaneously with either higher or lower illumination intensities in $I_{SI}(\vec{r})$, which now falls safely with the limited DR of the camera. To quantify the object's true fluorescent distribution $O(\vec{r})_{HDR}$, the effect of the spatially varying illumination pattern can be normalized to obtain,

$$O(\vec{r})_{HDR} = \frac{I_{SI}(\vec{r}_1)}{[\alpha(\vec{r}_1) \cdot P] * PSF} + \frac{I_{SI}(\vec{r}_2)}{P * PSF} + \frac{I_{SI}(\vec{r}_3)}{[\beta(\vec{r}_3) \cdot P] * PSF} \quad (5)$$

Figure 1 illustrates the principle of our SI-HDR method. In conventional HDR imaging, different ranges of luminance are captured by sequentially taking short and long exposure images under homogeneous illumination. When the object of interest emits a broad range of light intensities, the short exposure image fails to detect faint structures while the long exposure image is saturated in strong light emitting regions as shown in Figs. 1a-d. To optimize the HDR reconstruction, exposures for each acquisition must be optimized and in practice 3 to 4 different images are usually taken for solid reconstruction. In contrast, by modulating the illumination light intensity as an inverse function of the object's original intensity distribution, a single image can contain detailed morphological information beyond the limited DR of the detector. An example of such a SI pattern and the captured image is shown in Figs. 1e, and f, respectively. The object of interest is now illuminated by a customized distribution of light that results in optimal shot noise limited signal levels near the full well capacity limit of the detector for most effective pixels. Since we know the SI pattern that was illuminating the sample, the true fluorescence distribution of the object can be easily recovered using eqn. 5 as shown in Figs. 1g, and h. The recovered image clearly shows morphological structures that were previously concealed either by read noise or saturation in Figs. 1a-d (see Fig. S1 for quantitative analysis using fluorescent beads with largely varying differing intensities).

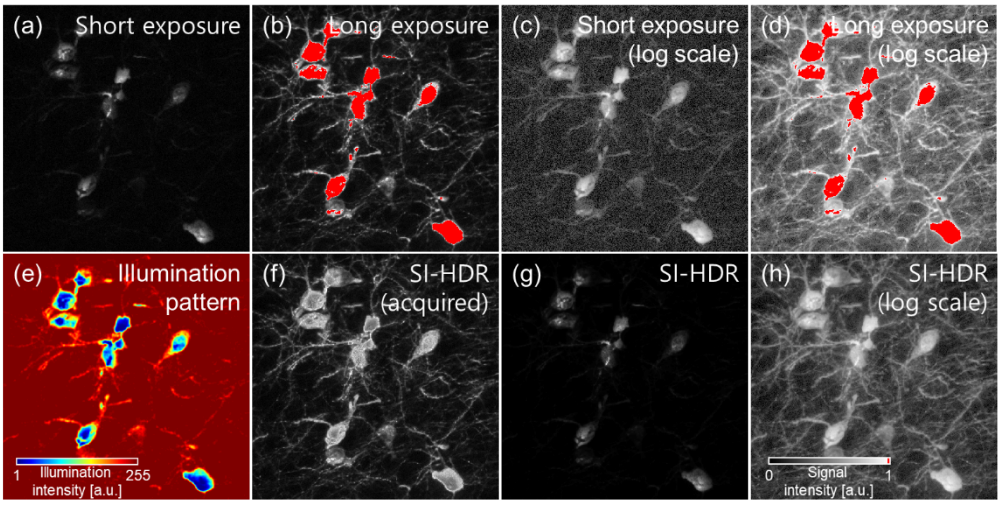

Fig. 1. Numerical simulation results of SI-HDR. (a) Short exposure, and (b) long exposure images of neurons in a mouse brain slice. Saturated pixels are shown in red. (c,d) Log scale images of Fig. 1a, and 1b, respectively. (e) SI-HDR illumination pattern optimizing fluorescence emission distribution. (f) SI-HDR acquired raw data. Reconstructed HDR image in (g) linear, and (h) log scale, using the data in Fig. 1e, and 1f. We can see that the fully recovered HDR range goes well beyond the 8 bit-depth resolution of common monitors or printers.

To illustrate the strengths and general applicability of SI-HDR in multimodal imaging applications, we built a DMD based widefield illumination system as shown in Fig. 2. We employed high power blue and green LEDs (SOLIS-470C, LED4D254, Thorlabs) with appropriate filter sets (ET525/50m, ZT488rdc-UF3, and ET500lp for GFP, and YFP, ET539/21x, ZT568rdc-UF1, FF01-607/70-25 for mCherry) for fluorescence imaging. A DMD (DLP6500EVM, Texas instruments) was positioned at a conjugate image plane to directly modulate the illumination pattern intensity. The resulting fluorescence emission was detected by a sCMOS camera (Zyla 4.2, Andor) with the PreAmpGainControl option set for low noise mode (12-bit). For diffraction limited accuracy in modulating the SI-HDR illumination pattern, image registration was carried out to obtain pixel-level alignment between the DMD illumination pattern and the acquired images on the camera (Fig. S2).

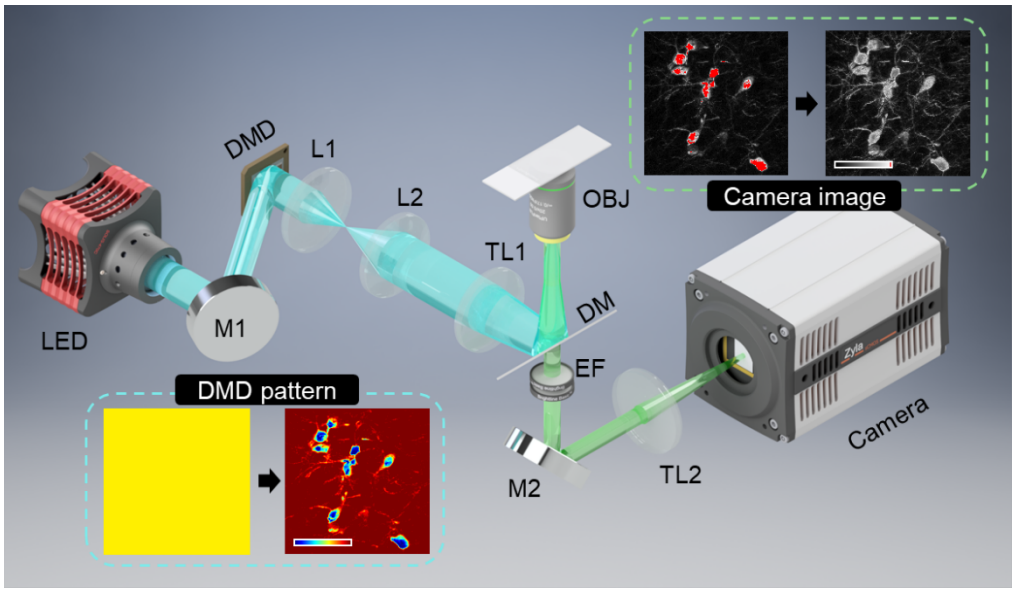

Fig. 2. Optical schematic of SI-HDR imaging system. Illumination intensity patterns on a DMD were updated in real-time by identifying noise dominated and saturated regions in the acquired images. M, mirror; DMD, digital micro-mirror device; L, lens; TL, tube lens; DM, dichroic mirror; OBJ, objective lens; EF, emission filter. Focal lengths of L1, L2, TL1, and TL2 are 400, 750, 300, and 180 mm, respectively.

3. Results and Discussion

Neuronal mitochondria segmentation

To highlight the quantitative nature of SI-HDR imaging in imaging both weak and strong intrinsic signal levels in a single image, we first imaged mitochondria in fixed cultured cortical neurons. Neuronal mitochondria are distributed throughout the entire cell with varying morphological features at each domain, such as soma, dendrites, and axons [34-36]. In general, high density of mitochondria with elongated shapes and large volume can be seen in somas and proximal dendrites, generally <150 μm from the soma, which results in bright signal levels in fluorescence images. On the other hand, axonal mitochondria and distal dendritic mitochondria, located >250 μm from the soma, are comparably shorter with smaller volumes and are sparsely located thus emitting much lower levels of fluorescence [34-38]. Recent works have shown that morphological structure of mitochondria along the neuron can help us understand the progress of neurodegenerative diseases such as Alzheimer's and Parkinson's diseases [39-41]. But to visualize the mitochondria over the entire cell simultaneously, which emit different amounts of fluorescence, previous research resorted to using higher illumination intensities or longer exposure times which saturates the mitochondrial signal in the soma and dendrites [42, 43].

Here we demonstrate that SI-HDR can provide an answer to these difficulties and enable the quantification of morphological subcellular features and density of mitochondria in entire

neurons. We performed SI-HDR on cultured cortical pyramidal neurons where mitochondria were labelled with YFP. To identify axons versus dendrites and verify the image enhancement, we also loaded the pyramidal neurons with mCherry as a filler so that axons can be identified by thin processes and the lack of spines. Figure 3 shows the imaging results for conventional imaging and SI-HDR. In conventional imaging (Fig. 3a), weak homogeneous illumination enables the detection of mitochondria in the soma and proximal dendrites, but fluorescence signal from axonal and distal dendritic mitochondria could not be sufficiently captured. On the other hand, strong homogeneous illumination successfully visualizes weakly fluorescing mitochondria in the axon and distal dendrites as shown in Fig. 3b but results in saturation for mitochondria in the soma and proximal dendrite regions. In stark contrast, fluorescence signals can be quantitatively measured from all regions of the neuron regardless of the size and density of mitochondria using SI-HDR (Fig. 3c). All results in Fig. 3 are shown after applying gamma correction by a factor of 0.3 for visibility on a standard monitor or printer. Large densely populated mitochondria in the soma and smaller mitochondria sparsely populated in the axon and distal dendrites could be quantitatively observed simultaneously only in the SI-HDR images (Fig. 3c,d). Using previously published mitochondrial segmentation algorithms [18, 44], we found that mitochondria in all neuronal regions including soma, dendrites, and axon were clearly identified only in SI-HDR images (Fig 3e). We also performed additional manual segmentation for somatic mitochondria due to the irregular shapes that were not successfully segmented via automatic image processing alone. We next classified the segmented mitochondria with respect to the location of each individual mitochondrion and visualized them with different colors as shown in Fig. 3f. We could verify dense mitochondria with complex structures in soma (cyan), sparsely distributed large mitochondria in dendrites (green), and thin and short mitochondria in axons (orange), corresponding to high, intermediate, and low signal intensities in SI-HDR images, respectively. Long and large mitochondria emit stronger fluorescence compared to short and tiny mitochondria in general. Thus, conventional imaging using either weak or strong illumination resulted in lower counts of segmented mitochondria with comparably smaller or larger sizes, respectively (Fig. 3g). In comparison, SI-HDR image analysis resulted in the highest total mitochondria count as all mitochondria were measured with sufficient SNR irrespective of the location of each mitochondrion. We can also see that the total number of smaller mitochondria agrees well for the strongly illuminated and SI-HDR images whereas the total number of larger mitochondria agrees well for the weakly illuminated and SI-HDR images as expected. The intermediate size mitochondria number agreed overall for all images except for the weak illumination image incorrectly identifying slightly smaller number of mitochondria in the dendrites.

We next quantified signal intensity distribution in Figs. 3a, and c, in linear and log scaled histograms as shown in Fig. 3h and i, respectively. In the linear scaled histogram (Fig. 3h), seemingly little difference was observed between the two images. However, by observing the log scaled histogram (Fig. 3i), we can see that the SI-HDR image has no saturated pixels and also contains drastically larger number of pixels ranging from 0 to 5-bit signal levels that were successfully measured above the noise floor (electronic read noise) compared to when using conventional homogenous illumination. The higher SNR over the entire FOV results in successful segmentation of all mitochondria across different neuronal regions enabling quantification of the number, size, and signal intensity according to each mitochondria location (Fig. 3f).

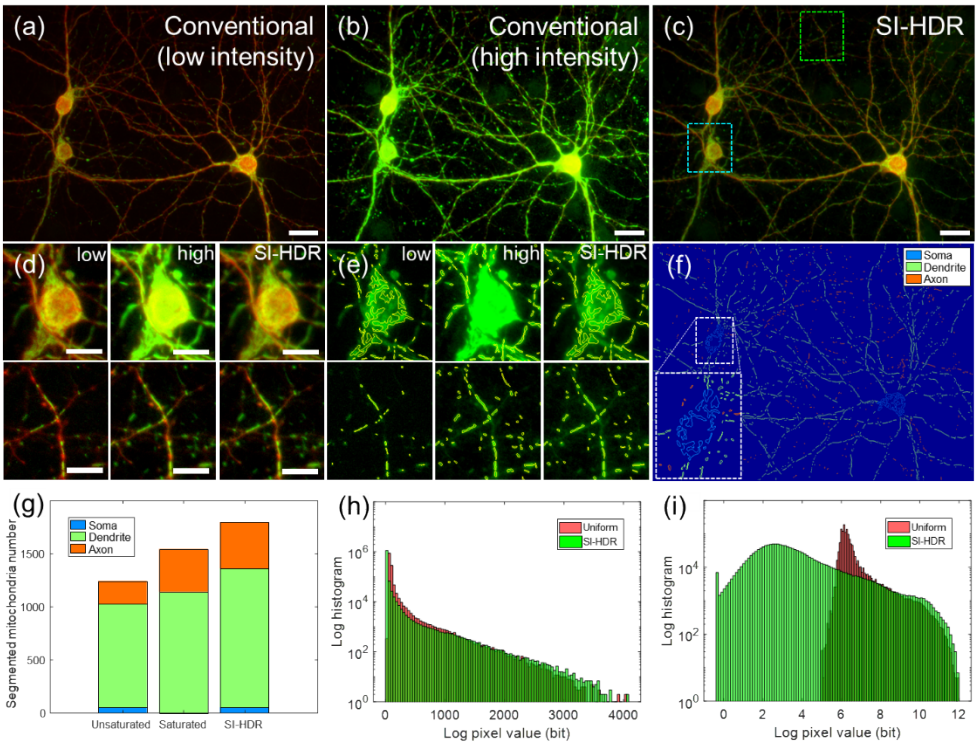

Fig. 3. Mitochondria segmentation in cultured neurons. Mitochondria labeled with YFP was imaged with varying illumination methods while the neuronal cytoplasm labeled with mCherry was obtained using a single constant illumination and overlayed. Images obtained with homogeneous illumination with intensities (a) just below saturation, (b) above saturation, and (c) SI-HDR. (d) Magnified mitochondria images, and (e) segmentation results of square regions marked in Figs. 3c with cyan, and green dotted squares. Whereas low and high intensity homogeneous illuminations result in successful segmentation for the somatic, and distal dendrite regions, respectfully, SI-HDR permits successful segmentation for all regions. (f) Mitochondria segmentation result in Fig. 3c, classified by the location of each mitochondrion. (g) Segmented mitochondria counts per the location. Respective signal intensity histograms in (h) linear, and (i) log scales. Scalebars; 20 μm, and 10 μm in (a-c), and (d), respectively.

Fast SI-HDR whole brain slice imaging

Investigating the morphofunctional connectivity of neuronal networks can provide important information in understanding the neuropathology of various neurodegenerative diseases and psychiatric disorders [45-47]. Image analysis of brain slices from animal models is therefore a gold standard for understanding the structural and cellular/subcellular changes of brain in neurological disorders [45-49]. To improve the accuracy of connectivity analysis, we should acquire correct morphological information of both neuronal processes and somas

simultaneously. The difficulty again arises from the fact that the limited DR of conventional detectors compromises accurate signal measurements arising from such varying regions. The problem becomes even worse when imaging large volumes of brain tissue as cell type, shape, density, and the resulting fluorescence yield varies widely across the brain. As it is not trivial to set an optimal illumination intensity or exposure time for the entire brain, common practice is to induce high illumination flux to visualize weakly fluorescing structures which results in saturation of many brain areas. Furthermore, a large acquisition time is necessary for high resolution gigapixel imaging of entire brain slices which restricts practical application of conventional HDR techniques due to their multi-acquisition nature [50-52].

SI-HDR offers a great advantage for such type of task as the imaging speed is identical with conventional widefield imaging. Although SI-HDR requires a single prior image to identify the approximate fluorescence distribution of the object, consequent imaging uses the prior SI-HDR imaging result to track the object of interest. In other words, an initial latency of one image is required but the following actual imaging speed is not compromised which enables the dynamic SI-HDR imaging. A similar principle was used to enable high throughput SI-HDR mosaicking of multiple image stitches to image a whole brain slice. A sample stage (MS-2000, ASI) was used to stitch multiple different FOVs. We found that while the sample stage is moving to the next position of interest, the speed is decreased slightly before reaching and stopping at the final position. We exploited this time window during the 'dead time' of sample stage scanning to realize the same imaging throughput as conventional widefield imaging. SI-HDR patterns were calculated based on an image obtained in the short time window immediately before the sample stage stopped at each tile location (see Materials and Methods and Supplementary Fig. S5 for detailed information regarding synchronization of the light source, sample stage, DMD, and camera). By taking advantage of the dead time during sample stage movement, SI-HDR mosaicking of an entire brain slice took exactly the same amount of time as stitching conventional widefield images which is the fastest and easiest stitching method to date.

Using SI-HDR, we imaged a 20 μm thick coronal sectioned mouse brain slice of a Thy1-YFP mouse that was additionally labeled with GFP antibody to match our illumination source spectrum. The entire brain slice was imaged while SI-HDR automatically adapted to neuromorphological features across the whole mouse brain slice. We acquired the morphological features of a whole brain slice by combining 62 x 42 tiles in total. Each tile was composed of 1024 x 1024 pixels with an effective camera pixel size of 162.5 nm which is below half of the diffraction limit (427 nm) of our system. The image tiles were stitched using the 'Stitching' plugin in imageJ [53]. Whole brain SI-HDR imaging was easily realized without any human intervention as shown in figure 4. The total pixel number of the stitched image was approximately 1.8 gigapixels (50983 x 34603). As previously mentioned, the total measurement time was the same as it takes for mosaic stitching using conventional widefield imaging. However, the information content and quality of SI-HDR far exceeds that achievable in conventional widefield imaging where fine structures such as dendritic spines that were obscured with noise can now clearly be seen. We can easily see the large variation in signal levels across the brain slice when illuminating the entire brain with a constant homogeneous illumination; for example, soma in primary somatosensory cortex, and basolateral amygdala (BLA) regions show much stronger fluorescence than other regions (Fig. 4a) due to the

difference in Thy1-YFP expression [54, 55]. Here, the incident light intensity was adjusted so that the maximum fluorescence at Thy1-expressing neurons of BLA regions were measured just below saturation to fully utilize the camera dynamic range. Thus, degradation of SNR is inevitable in other regions where weaker fluorescing structures are dominant. In comparison, the acquired image using SI-HDR shows a homogeneous signal level for all regions of the entire mouse brain slice as shown in Fig. 4b. Therefore, all structures can be simultaneously measured up to the shot noise limit. The measured SI-HDR raw data where all measured data points are now boosted above the noise floor is then quantitatively normalized by the SI illumination pattern (Fig. 4c) and eqn. 5 as shown in Fig. 4d. Due to the limited dynamic range of modern displays, the SI-HDR image looks similar with conventional uniform illumination imaging in linear scale. However, we could verify significant differences in the weakly fluorescing regions such as dendritic spines in the neocortex (Fig. 4e) by selectively displaying pixels according to signal levels that were not measured in conventional imaging (pixels highlighted with the blue dotted square in Fig. 4f). Magnified images of the regions marked by the red dotted squares in Fig. 4e were further compared by obtaining 9 μm thick z-stack volumes (maximum intensity projections (MIPs) shown in Figs. 4g, and 4h, respectively). Both thin dendrite and tiny spines emitting weak fluorescent signal was clearly observed in SI-HDR images, which were covered with noise using uniform illuminations (Supplementary Movie 1). We next performed 3D deconvolution process using commercial deconvolution software (AutoQuantX2, Media Cybernetics, Inc.) to demonstrate the advantage in background signal suppression. Due to the low SNR, no significant difference was obtained through deconvolution using data acquired with uniform illumination (Fig. 4i). In contrast, fine neuronal structures were clearly observed using the deconvolved SI-HDR image data (Fig. 4j), which was originally hidden behind the out-of-focus blur.

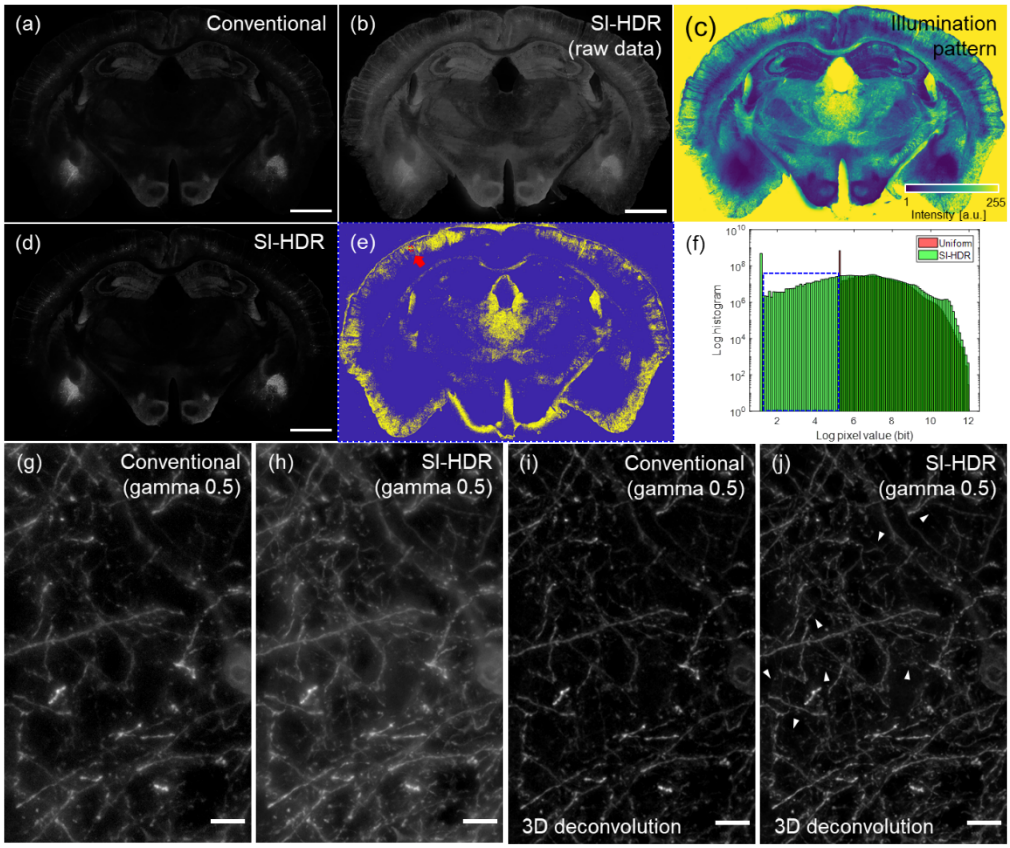

Fig. 4. SI-HDR whole mouse brain slice imaging. Raw data of 20 μm thick mouse brain slice acquired with (a) uniform illumination intensity, and (b) SI-HDR illumination. (c) SI-HDR illumination pattern, and (d) reconstructed HDR image using Figs. 4b, and 4c. (e) Signal intensity enhanced region (yellow) corresponding to signal intensity range marked by the dotted blue square in (f) log scaled pixel histogram. (g,h) Magnified gamma (0.5) rescaled images of 9 μm thick volume MIPs of the red boxed regions the primary somatosensory cortex in Fig. 4e. (i,j) Deconvolution results of Figs. 4g,h. Arrows are guides to the eye pointing to dendritic spines that are clearly observed with enhanced SNR. Scalebars; 1000 μm, 10 μm in (a,b,d), and (g-j), respectively.

SI-HDR HiLo for depth sectioned HDR imaging

Although we demonstrated that SI-HDR can effectively increase the DR for thin biological samples such as cultured neurons or thin brain slices, SI-HDR itself does not have depth sectioning capabilities which is required for volumetric imaging where the out of focus background ruins the information content. This can also be seen in Fig. 4 where the out of focus background reduces the image contrast even for the relatively thin 20 μm thin brain slice. Fortunately, SI-HDR can be applied to all SI or widefield imaging methods in general. Exploiting the general applicability of SI-HDR, we realized depth selective HDR imaging by adapting the concepts of HiLo microscopy to incorporate SI-HDR HiLo microscopy [31-33]. In brief, the sinusoidal illumination pattern in HiLo was additionally modulated to adapt to the

sample fluorescence intensity distribution. Ideally, the acquired image will be a perfect grid pattern which is then processed using the SI-HDR HiLo illumination pattern to obtain the true data used for HiLo reconstruction. Experimentally, we chose to use light intensities according to DMD index ranges between 8-128 for the volumetric imaging using HiLo structured illumination. The range of intensities utilized for the structured illumination was empirically chosen to reduce photobleaching of out- of-focus planes and to obtain a sufficient modulation contrast even for the weakest illuminations.

To verify enhancement in depth sectioning capabilities, we prepared a 100 µm thick slice of GFP stained mouse brain and imaged a 990 x 990 µm2 area in the hippocampus. For comparison, we obtained images with conventional widefield imaging (Fig. 5a), HiLo (Fig. 5b), and SI-HDR HiLo (Fig. 5c). As expected, conventional widefield imaging suffers from both the limited DR and out of focus background (Fig. 5a, d). HiLo shows improvement in suppressing the out of focus background but suffers from limited DR. Furthermore, we can also see limitations of HiLo especially when there is saturation or at low signal levels. Both signal saturation and low signal levels results in an incorrect sinusoidal intensity modulation which is required for HiLo reconstruction and therefore fails to discriminate structures that were at different depths due to either noisy or saturated signals in the data. In contrast, using SI-HDR HiLo (Fig. 5c, f), we can see correct depth sectioning for structures that failed to be detected using conventional HiLo (Supplementary Movie 2).

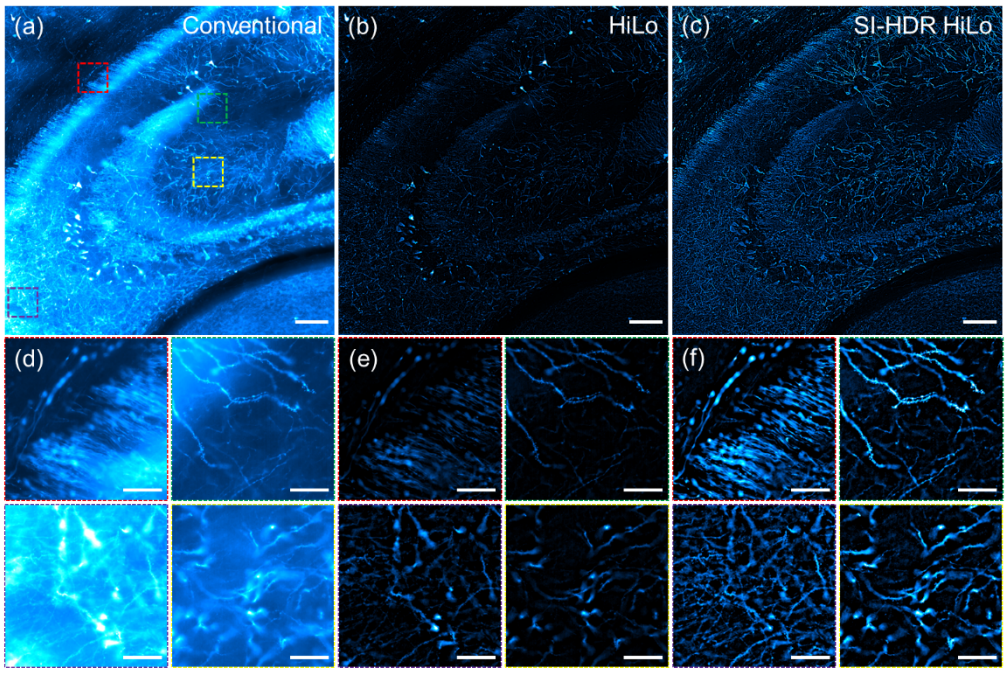

Fig. 5. SI-HDR HiLo for high resolution depth sectioned imaging. 100 µm thick opaque mouse brain slice image captured by (a) WF, (b) HiLo, and (c) SI-HDR HiLo. (d-f) Magnified images of corresponding highlighted ROIs for the respective images. Scalebars; 100 µm, and 20 µm in (a-c), and (d-f), respectively.

3D reconstruction using SI-HDR HiLo

Encouraged by the enhanced depth sectioning results using SI-HDR, we next performed 3D HDR imaging. Here, the SI pattern was adaptively adjusted automatically per depth based on image collected from a single prior widefield image. This procedure was again performed while the sample stage was moving, and the total 3D volume acquisition time was therefore identical to when using conventional HiLo imaging. 3D imaging was performed on a 120 μm thick coronal section in the hippocampus area of an optically cleared Thy1-YFP mouse brain. To compare 3D reconstructed results, we obtained conventional HiLo images using relatively low illumination intensities (Figs. 6a) with homogeneous illumination just below saturation, and SI-HDR HiLo imaging in 500 nm z-steps using a piezo sample stage (Fig. 6b). The 3D reconstructions were rendered using the commercial software Imaris.

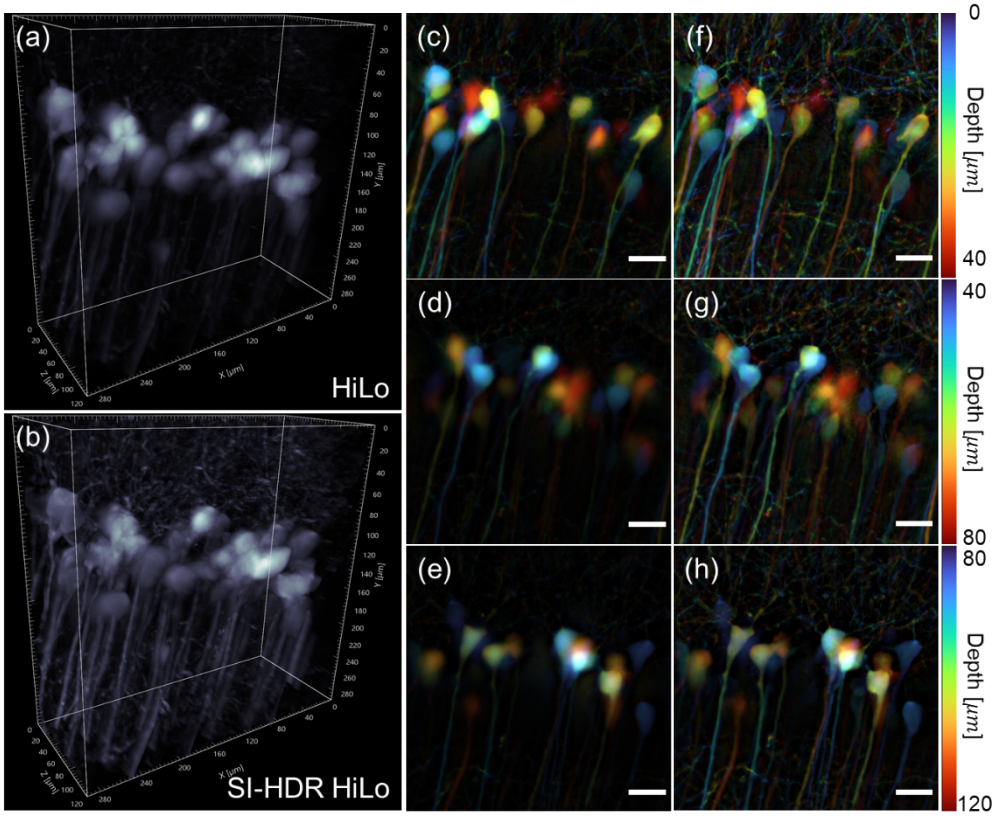

Fig. 6. Depth sectioned images with the HiLo microscopy. 3D reconstruction of hippocampal pyramidal neurons of 120 μm thick coronal sectioned optically cleared mouse brain obtained by (a) conventional HiLo and (b) SI-HDR HiLo, respectively. Maximum intensity projection (MIP) images of 40 μm thick volumes descending from the surface measured by (c-e) conventional HiLo and (f-h) SI-HDR HiLo, respectively. Scalebar; 20 μm.

Optically sectioned image blocks of 40 μm thickness centered at corresponding depths (20, 60, 100 um) are shown in Figs. 6c-6h and Supplementary Movie 3. At each according block of tissue, a large proportion of highly varying complex structures across the FOV were only identifiable in the SI-HDR HiLo results (Fig. 6f-h). In general, HiLo microscopy has a speed ~10 times faster than that of conventional confocal microscopy that is currently widely used for optically sectioned 3D imaging [31]. In confocal microscopy, limitations due to the limited DR is actually more severe due to the narrower DR of photomultiplier tubes compared to sCMOS sensors. Commercial confocal microscopes therefore often also have HDR imaging options which take multiple image acquisitions using different illumination intensities or different pixel dwell times. This, however, slows down the already slow framerate and also increases photobleaching. In our current demonstration, the 3D image stack using SI-HDR HiLo takes the same amount of time as conventional HiLo imaging (two images per depth plane). We expect that SI-HDR can be especially useful for fast high resolution imaging of large optically cleared tissues which are rapidly becoming available but face difficulties in direct application of laser scanning optical sectioning methods due to their slow speed.

4. Conclusion

We demonstrated SI-HDR microscopy that can expand the DR by modulating incident light intensity into arbitrary high resolution illumination patterns customized to the object of interest by simply adding a DMD to a conventional widefield microscope. Extended DR imaging was demonstrated on cultured neurons and thin/thick mouse brain slices with high variability in fluorescence distribution. We found the method to be especially useful for high-throughput high dynamic range microscopy such as large FOV stitching or large volume 3D imaging. Here, the SI-HDR illumination pattern could be identified during the sample stage movement cycle enabling the total acquisition time to be maintained the same as in conventional widefield imaging.

Although our current implementation focused on HDR imaging for high throughput imaging of static samples, the method can also be applied for dynamic functional imaging. For example, in calcium imaging, detecting a single action potential is difficult due to the small increase in fluorescence signal. Since SI-HDR imaging can adapt the illumination pattern in millisecond time scales including all the processing steps including camera acquisition, pattern calculation, and pattern illumination, SI-HDR can potentially follow the transient calcium dynamics for a single action potential. Successful realization of such a scheme will potentially help identify neuronal signals that were previously undetected.

Our current implementation of SI-HDR realized pixel by pixel alignment of the DMD and sCMOS camera on a pixel-by-pixel scale resolution. The optimal resolution of SI-HDR can be further exploited by incorporating additional SI imaging techniques such as super-resolution SIM using the identical experimental setup [56]. As we demonstrated in HiLo, super-resolution SIM is also known to be prone to artifacts related to low signal levels which can potentially benefit from SI-HDR. The degree of alignment can of course be relaxed if the level of resolution required is not high.

In conclusion, we demonstrated SI-HDR microscopy which automatically adapts to the sample of interest to extend the DR. The method is broad and general and can be directly applied to replace conventional widefield imaging methods. Using SI-HDR, we realized high resolution quantitative analysis of mitochondria distributions that vary in both shape and density throughout extended structures of neurons. The high quality HDR information content enabled automatic segmentation of mitochondria with much higher accuracy in comparison with conventional widefield imaging using the same segmentation algorithm and demonstrated efficient collection of neuronal mitochondria morphological information. A recent study using 3D electron microscopy (EM) showed that mitochondrial shapes of neuronal compartments are different depending on subregions of mouse brains, and that age-related morphological changes are region- and compartment-specific [57]. However, EM sampling consumes considerably longer amounts of time than fluorescence sample preparation and imaging, and has limitations for defining different neuron types and in covering large imaging areas. Therefore, SI-HDR may be a method of choice for quantitative whole neuronal mitochondrial quantitative imaging without the hassles of intensity adjustments and multiple acquisitions per specific subregions and cell-types while still benefiting from simpler sample preparation steps and image analysis.

Since the SI-HDR illumination can be realized in real time using a fast DMD, we further realized highly efficient HDR acquisition for high throughput gigapixel scale imaging of whole mouse brain slice as well as fast depth sectioned 3D volumetric SI-HDR imaging demonstrating its expandability. Importantly, highly varying morphological features in SI-HDR images could be captured in the same total acquisition time as conventional widefield imaging, in comparison, traditional widefield HDR imaging requires multiple image acquisitions where the total extended DR is decided by the number of acquisitions. The method is general and simple to implement which can bring wide dissemination of the method for a broad range of applications. We envision that SI-HDR can open a new window for discovery of new biological phenomena that were previously unobservable due to hardware DR limitations.

Funding. National Research Foundation of Korea (2017M3C7A1044966, 2019M3E5D2A01063812, 2019M3E5D2A01063794, 2020R1A6A3A01097999, 2021R1A2C3012903, 2021R1A4A1031644), and the TJ Park Foundation.

Disclosures. The authors declare no conflicts of interest.

Data availability. Data underlying the results presented in this paper are not publicly available at this time but may be obtained from the authors upon reasonable request.

Supplemental document. See Supplement 1 for supporting content.

5. References

1. J. M. Paul E. Debevec, "Recovering High Dynamic Range Radiance Maps from Photographs," Proc. of ACM SIGGRAPH 1997, 369-378 (1997).
2. M. U. Sing Bing Kang, Simon Winder, and Richard Szeliski, "High dynamic range video," ACM Transactions on Graphics (TOG) **22**, 319-325.
3. T. Jinno and M. Okuda, "Multiple exposure fusion for high dynamic range image acquisition," IEEE Trans Image Process **21**, 358-365 (2012).

4. S. Li, "Fast Multi-exposure Image Fusion with Median Filter and Recursive Filter," IEEE Transactions on Consumer Electronics **58**, 626-632 (2012).
5. I. Merianos and N. Mitianoudis, "Multiple-Exposure Image Fusion for HDR Image Synthesis Using Learned Analysis Transformations," Journal of Imaging **5**(2019).
6. a. T. M. Shree K. Nayar, "High Dynamic Range Imaging: Spatially Varying Pixel Exposures," IEEE **1**(2000).
7. S. K. Nayar, and Vlad Branzoi, "Adaptive dynamic range imaging: Optical control of pixel exposures over space and time," Proceedings of the Ninth IEEE International Conference on Computer Vision (ICCV'03) (2003).
8. J. W. Lichtman and J. A. Conchello, "Fluorescence microscopy," Nat Methods **2**, 910-919 (2005).
9. T. W. Chen, T. J. Wardill, Y. Sun, S. R. Pulver, S. L. Renninger, A. Baohan, E. R. Schreiter, R. A. Kerr, M. B. Orger, V. Jayaraman, L. L. Looger, K. Svoboda, and D. S. Kim, "Ultrasensitive fluorescent proteins for imaging neuronal activity," Nature **499**, 295-300 (2013).
10. H. Dana, Y. Sun, B. Mohar, B. K. Hulse, A. M. Kerlin, J. P. Hasseman, G. Tsegaye, A. Tsang, A. Wong, R. Patel, J. J. Macklin, Y. Chen, A. Konnerth, V. Jayaraman, L. L. Looger, E. R. Schreiter, K. Svoboda, and D. S. Kim, "High-performance calcium sensors for imaging activity in neuronal populations and microcompartments," Nat Methods **16**, 649-657 (2019).
11. N. C. Shaner, M. Z. Lin, M. R. McKeown, P. A. Steinbach, K. L. Hazelwood, M. W. Davidson, and R. Y. Tsien, "Improving the photostability of bright monomeric orange and red fluorescent proteins," Nat Methods **5**, 545-551 (2008).
12. R. Rizzuto, M. Brini, F. De Giorgi, R. Rossi, R. Heim, R. Y. Tsien, and T. Pozzan, "Double labelling of subcellular structures with organelle-targeted GFP mutants in vivo," Curr Biol **6**, 183-188 (1996).
13. R. A. Hoebe, C. H. Van Oven, T. W. Gadella, Jr., P. B. Dhonukshe, C. J. Van Noorden, and E. M. Manders, "Controlled light-exposure microscopy reduces photobleaching and phototoxicity in fluorescence live-cell imaging," Nat Biotechnol **25**, 249-253 (2007).
14. H. T. M. V. D. V. R.A. HOEBE, J. STAP, C.J.F. VAN NOORDEN, E.M.M. MANDERS, "Quantitative determination of the reduction of phototoxicity and photobleaching by controlled light exposure microscopy," Journal of Microscopy **231**, 9–20 (2008).
15. R. Yang, T. D. Weber, E. D. Witkowski, I. G. Davison, and J. Mertz, "Neuronal imaging with ultrahigh dynamic range multiphoton microscopy," Sci Rep **7**, 5817 (2017).
16. D. L. Kengyeh K. Chu, and Jerome Mertz, "Practical implementation of log-scale active illumination microscopy," BIOMEDICAL OPTICS EXPRESS **1**, 236-245 (2010).
17. D. L. Kengyeh K. Chu, and Jerome Mertz, "Enhanced weak-signal sensitivity in two-photon microscopy by adaptive illumination," OPTICS LETTERS **32**, 2846-2848 (2007).
18. C. Vinegoni, C. Leon Swisher, P. Fumene Feruglio, R. J. Giedt, D. L. Rousso, S. Stapleton, and R. Weissleder, "Real-time high dynamic range laser scanning microscopy," Nat Commun **7**, 11077 (2016).
19. C. Vinegoni, P. F. Feruglio, and R. Weissleder, "High dynamic range fluorescence imaging," IEEE Journal of Selected Topics in Quantum Electronics **25**, 1-7 (2018).
20. P. F. Feruglio, C. Vinegoni, and R. Weissleder, "Extended dynamic range imaging for noise mitigation in fluorescence anisotropy imaging," Journal of Biomedical Optics **25**, 086003 (2020).
21. P. T. Van, V. Bass, D. Shiwarski, F. Lanni, and J. Minden, "High dynamic range proteome imaging with the structured illumination gel imager," Electrophoresis **35**, 2642-2655 (2014).
22. L. Schermelleh, R. Heintzmann, and H. Leonhardt, "A guide to super-resolution fluorescence microscopy," J Cell Biol **190**, 165-175 (2010).
23. A. A. Adeyemi, N. Barakat, and T. E. Darcie, "Applications of digital micro-mirror devices to digital optical microscope dynamic range enhancement," Optics Express **17**, 1831-1843 (2009).
24. P. T. Van, V. Bass, D. Shiwarski, F. Lanni, and J. Minden, "High dynamic range proteome imaging with the structured illumination gel imager," Electrophoresis **35**, 2642-2655 (2014).
25. S. K. Nayar and V. Branzoi, "Adaptive dynamic range imaging: Optical control of pixel exposures over space and time," in *Proceedings Ninth IEEE International Conference on Computer Vision*, (IEEE, 2003), 1168-1175.
26. S. K. Nayar, V. Branzoi, and T. E. Boult, "Programmable imaging using a digital micromirror array," in *Proceedings of the 2004 IEEE Computer Society Conference on Computer Vision and Pattern Recognition, 2004. CVPR 2004.*, (IEEE, 2004), I-I.
27. M. Abolbashari, F. Farahi, F. Magalhaes, F. M. Araújo, and M. V. Correia, "High dynamic range compressive imaging: a programmable imaging system," Optical Engineering **51**, 071407 (2012).
28. S.-B. Zhao, L.-Y. Liu, and M.-Y. Ma, "Adaptive high-dynamic range three-dimensional shape measurement using DMD camera," IEEE Access **7**, 67934-67943 (2019).
29. O. Bimber, D. Klöck, T. Amano, A. Grundhöfer, and D. Kurz, "Closed-loop feedback illumination for optical inverse tone-mapping in light microscopy," IEEE Transactions on Visualization and Computer Graphics **17**, 857-870 (2010).
30. Y. Qiao, X. Xu, T. Liu, and Y. Pan, "Design of a high-numerical-aperture digital micromirror device camera with high dynamic range," Applied optics **54**, 60-70 (2015).
31. D. Lim, T. N. Ford, K. K. Chu, and J. Metz, "Optically sectioned in vivo imaging with speckle illumination HiLo microscopy," Journal of biomedical optics **16**, 016014 (2011).

32. J. Schniete, A. Franssen, J. Dempster, T. J. Bushell, W. B. Amos, and G. McConnell, "Fast optical sectioning for widefield fluorescence mesoscopy with the mesolens based on HiLo microscopy," Scientific reports **8**, 1-10 (2018).
33. Q. Zhang, D. Pan, and N. Ji, "High-resolution in vivo optical-sectioning widefield microendoscopy," Optica **7**, 1287-1290 (2020).
34. Z. Li, K.-I. Okamoto, Y. Hayashi, and M. Sheng, "The importance of dendritic mitochondria in the morphogenesis and plasticity of spines and synapses," Cell **119**, 873-887 (2004).
35. M. E. Chicurel and K. M. Harris, "Three-dimensional analysis of the structure and composition of CA3 branched dendritic spines and their synaptic relationships with mossy fiber boutons in the rat hippocampus," Journal of comparative neurology **325**, 169-182 (1992).
36. T. L. Lewis, S.-K. Kwon, A. Lee, R. Shaw, and F. Polleux, "MFF-dependent mitochondrial fission regulates presynaptic release and axon branching by limiting axonal mitochondria size," Nature communications **9**, 1-15 (2018).
37. A. S. Dickey and S. Strack, "PKA/AKAP1 and PP2A/Bβ2 regulate neuronal morphogenesis via Drp1 phosphorylation and mitochondrial bioenergetics," Journal of Neuroscience **31**, 15716-15726 (2011).
38. T. L. Lewis Jr, J. Courchet, and F. Polleux, "Cellular and molecular mechanisms underlying axon formation, growth, and branching," Journal of Cell Biology **202**, 837-848 (2013).
39. M. H. Yan, X. Wang, and X. Zhu, "Mitochondrial defects and oxidative stress in Alzheimer disease and Parkinson disease," Free Radical Biology and Medicine **62**, 90-101 (2013).
40. D. J. Bonda, X. Wang, H.-G. Lee, M. A. Smith, G. Perry, and X. Zhu, "Neuronal failure in Alzheimer's disease: a view through the oxidative stress looking-glass," Neuroscience bulletin **30**, 243-252 (2014).
41. S. Arun, L. Liu, and G. Donmez, "Mitochondrial biology and neurological diseases," Current neuropharmacology **14**, 143-154 (2016).
42. B. H. Varkuti, M. Kepiro, Z. Liu, K. Vick, Y. Avchalumov, R. Pacifico, C. M. MacMullen, T. M. Kamenecka, S. V. Puthanveettil, and R. L. Davis, "Neuron-based high-content assay and screen for CNS active mitotherapeutics," Science advances **6**, eaaw8702 (2020).
43. A. Sorvina, C. A. Bader, J. R. Darby, M. C. Lock, J. Y. Soo, I. R. Johnson, C. Caporale, N. H. Voelcker, S. Stagni, and M. Massi, "Mitochondrial imaging in live or fixed tissues using a luminescent iridium complex," Scientific reports **8**, 1-8 (2018).
44. R. J. Giedt, D. R. Pfeiffer, A. Matzavinos, C.-Y. Kao, and B. R. Alevriadou, "Mitochondrial dynamics and motility inside living vascular endothelial cells: role of bioenergetics," Annals of biomedical engineering **40**, 1903-1916 (2012).
45. E. Danielson and S. H. Lee, "SynPAnal: software for rapid quantification of the density and intensity of protein puncta from fluorescence microscopy images of neurons," PloS one **9**, e115298 (2014).
46. P. Verstraelen, M. Van Dyck, M. Verschuuren, N. D. Kashikar, R. Nuydens, J.-P. Timmermans, and W. H. De Vos, "Image-based profiling of synaptic connectivity in primary neuronal cell culture," Frontiers in neuroscience **12**, 389 (2018).
47. J. C. Fiala, J. Spacek, and K. M. Harris, "Dendritic spine pathology: cause or consequence of neurological disorders?," Brain research reviews **39**, 29-54 (2002).
48. D. Zhang, S. Liu, Y. Song, D. Feng, H. Peng, and W. Cai, "Automated 3D soma segmentation with morphological surface evolution for neuron reconstruction," Neuroinformatics **16**, 153-166 (2018).
49. W. C. Risher, T. Ustunkaya, J. S. Alvarado, and C. Eroglu, "Rapid Golgi analysis method for efficient and unbiased classification of dendritic spines," PloS one **9**, e107591 (2014).
50. A. Orth and K. B. Crozier, "High throughput multichannel fluorescence microscopy with microlens arrays," Optics express **22**, 18101-18112 (2014).
51. J. Chalfoun, M. Majurski, T. Blattner, K. Bhadriraju, W. Keyrouz, P. Bajcsy, and M. Brady, "Mist: accurate and scalable microscopy image stitching tool with stage modeling and error minimization," Scientific reports **7**, 1-10 (2017).
52. A. Orth, M. J. Tomaszewski, R. N. Ghosh, and E. Schonbrun, "Gigapixel multispectral microscopy," Optica **2**, 654-662 (2015).
53. S. Preibisch, S. Saalfeld, and P. Tomancak, "Globally optimal stitching of tiled 3D microscopic image acquisitions," Bioinformatics **25**, 1463-1465 (2009).
54. G. Feng, R. H. Mellor, M. Bernstein, C. Keller-Peck, Q. T. Nguyen, M. Wallace, J. M. Nerbonne, J. W. Lichtman, and J. R. Sanes, "Imaging neuronal subsets in transgenic mice expressing multiple spectral variants of GFP," Neuron **28**, 41-51 (2000).
55. C. Porrero, P. Rubio-Garrido, C. Avendaño, and F. Clascá, "Mapping of fluorescent protein-expressing neurons and axon pathways in adult and developing Thy1-eYFP-H transgenic mice," Brain research **1345**, 59-72 (2010).
56. T. Woo, S. Jeong, c. ahn, B. Hwang, h. kim, J. Kang, and J.-H. Park, "Tunable SIM: observation at varying spatiotemporal resolutions across the FOV," Optica (2020).
57. J. Faitg, C. Lacefield, T. Davey, K. White, R. Laws, S. Kosmidis, A. K. Reeve, E. R. Kandel, A. E. Vincent, and M. Picard, "3D neuronal mitochondrial morphology in axons, dendrites, and somata of the aging mouse hippocampus," Cell Rep **36**, 109509 (2021).